Large magnetoresistance and de Haas–van Alphen oscillations in the topological semimetal candidates BaX_4 (X=Ga, In)

Huan Wang,[1,2,*] Sheng Xu,[1,2,*] Xiao-Qin Lu,[1,*,†] Zheng-Yi Dai,[1,2] Yi-Yan Wang,[3] Xiao-Yan Wang,[1,2] Xiang-Yu Zeng,[1,2] Jun-Fa Lin,[1,2] Kai Liu,[1] Zhong-Yi Lu,[1] and Tian-Long Xia[1,2,‡]

[1]*Department of Physics, Renmin University of China, Beijing 100872, People's Republic of China*

[2]*Beijing Key Laboratory of Opto-electronic Functional Materials & Micro-nano Devices, Renmin University of China, Beijing 100872, People's Republic of China*

[3]*Institute of Physical Science and Information Technology, Anhui University, Hefei, Anhui 230601, China*

(Received 13 April 2021; accepted 25 October 2021; published 16 November 2021)

We report the magnetoresistance (MR), de Haas–van Alphen (dHvA) oscillations, and first-principles calculation studies on topological semimetal candidates BaX_4 (X=Ga, In). Large unsaturated MR that reaches 3×10^3% in $BaGa_4$ and 4×10^4% in $BaIn_4$ are observed, which is due to the carrier compensations and high mobility. Evident dHvA oscillations are detected with $B//[001]$ configuration, from which the quantum mobilities are extracted. The light cyclotron effective masses are extracted from the fitting of the thermal damping term in the LK formula. According to the first-principles calculations, BaX_4 possesses several Dirac points in the absence of spin-orbit coupling (SOC), some of which open negligible gaps when SOC is considered. The Z_2 invariants of BaX_4 are equal to 1, indicating the nontrivial topological properties.

DOI: 10.1103/PhysRevB.104.205119

I. INTRODUCTION

The study of topological materials which possess remarkable properties, such as high carrier mobility, large magnetoresistance (MR), nontrivial Berry phase, and chiral-anomaly-induced negative MR, has recently developed into an active area of research. Dirac and Weyl semimetals represent a significant advance in this field. In Dirac semimetals, of which Cd_3As_2 [1–6] and Na_3Bi [7–10] are the typical members, the fourfold degenerate band crossings appearing in the vicinity of the Fermi level are known as Dirac points, which disperse linearly along momentum directions [11]. Dirac semimetals are precursors to the so-called Weyl semimetals [12,13]. As the space inversion or time reversal symmetry is broken, Dirac semimetals evolve into Weyl semimetals, in which TaAs family [14–25] and $SrMnSb_2/YbMnPn_2$ (Pn= Sb and Bi) [26–29] are typical members. Thus, the search for new materials that carry novel characteristics lays a foundation for realizing exotic physical phenomena. Meanwhile, quantum oscillations provide an effective method for the identification of topological characteristics. The nontrivial Berry phases, high quantum mobility, and light effective masses, which are expected for topological characteristics, can be extracted from the analysis of quantum oscillations.

Recently, we reported the transition-metal aluminide $CaAl_4$ as a Dirac nodal line semimetal owning novel magnetotransport properties [30]. Further considering previous results and discussions [31–34], we grew the high-quality BaX_4 (X=Ga, In) single crystals with I_4/mmm space group. In this work, the magnetotransport measurements on BaX_4 combining with the first-principles calculations are reported. Large unsaturated MR that reaches 3×10^3% in $BaGa_4$ and 4×10^4% in $BaIn_4$ are observed, which is due to the carrier compensations and high mobility that may originate from topological nontrivial bands. Prominent de Haas–van Alphen (dHvA) quantum oscillations are detected with the $B//[001]$ configuration, from the analysis of which the multiple frequencies, light effective masses, and high quantum mobilities are extracted. Four/seven fundamental frequencies are extracted from the oscillations in $BaGa_4/BaIn_4$. Light effective masses are obtained from the fittings of the thermal damping term in Lifshitz-Kosevich (LK) formula, indicating the linear dispersion and the possible existence of massless Dirac fermions. High quantum mobilities in a range of $(0.1 \sim 6) \times 10^4$ cm^2 V^{-1} s^{-1} are obtained, indicating their possible nontrivial topological characteristics. The first-principles calculations indicate that there are several Dirac points in BaX_4 in the absence of spin-orbit coupling (SOC), some of which open negligible gaps in the presence of SOC. The Z_2 invariants of BaX_4 are equal to 1, indicating their nontrivial topological properties.

II. METHOD AND CRYSTAL STRUCTURE

The high quality single crystals of BaX_4 were grown by flux method. The mixture of Ba and X (X=Ga, In) elements with a ratio of 1:85 was loaded into corundum crucible which was sealed into a quartz tube. Then the tube was put into furnace and heated to 1100 °C for two days to allow melting and sufficient homogenization, then cooled down to 400 °C at a rate of 3 °C/h. Finally, crystals with metallic luster were obtained by centrifugation to remove excess flux at 400 °C. The

*These authors contributed equally to this paper.

†Present address: School of Physics and Information Engineering, Guangdong University of Education, Guangzhou, Guangdong 510303, China

‡tlxia@ruc.edu.cn

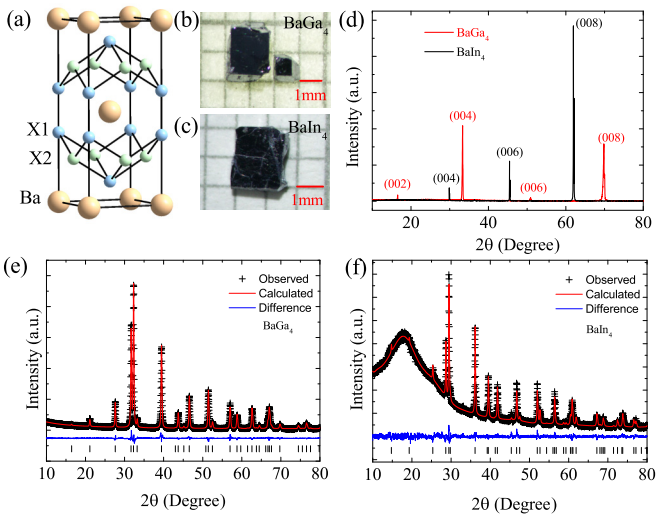

FIG. 1. (a) Crystal structure of BaX_4 with the space group $I4/mmm$ (No. 139). Pictures of grown single crystals of (b) $BaGa_4$ and (c) $BaIn_4$. (d) Single crystal XRD patterns of $BaGa_4$ and $BaIn_4$. Powder XRD patterns with refinement for (e) $BaGa_4$ and (f) $BaIn_4$.

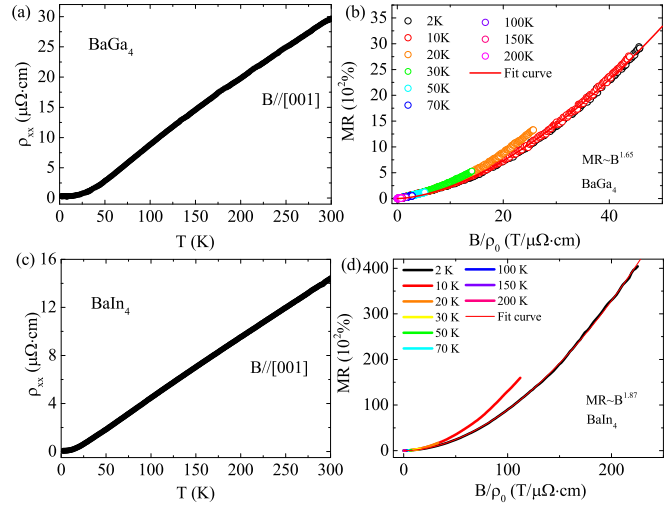

FIG. 2. The temperature-dependent resistivity curves from 2 K to 300 K of (a) $BaGa_4$ and (c) $BaIn_4$, respectively. The MR versus magnetic field at various temperatures with $B//[001]$ configuration for (b) $BaGa_4$ and (d) $BaIn_4$, respectively.

atomic composition was confirmed to be about Ba:X=1:4 by energy dispersive x-ray spectroscopy (EDS, Oxford X-Max 50). The single-crystal x-ray diffraction (XRD) patterns and powder XRD patterns were carried out by a Bruker D8 Advance x-ray diffractometer using Cu K_α radiation. TOPAS-4.2 was employed for the refinement. The measurements of resistivity and magnetic properties were performed on a Quantum Design physical property measurement system (PPMS-14T) and magnetic property measurement system (MPMS-3). The first-principles calculations were carried out with the projector augmented wave method [35,36] as implemented in the VASP package [37–39]. The generalized gradient approximation of Perdew-Burke-Ernzerhof type [40] was adopted for the exchange-correlation functional. The kinetic energy cutoff of the plane-wave basis was set to be 400 eV. The Brillouin zone was sampled with a $16 \times 16 \times 16$ k-point mesh. The Gaussian smearing method with a width of 0.01 eV was used for the Fermi surface (FS) broadening. Both lattice parameters and internal atomic positions were fully relaxed until all the forces became less than 0.01 eV/Å. The lattice constants of $BaGa_4$ ($a = b = 4.64$ Å, $c = 10.83$ Å) and $BaIn_4$ ($a = b = 5.06$ Å, $c = 12.21$ Å) were used for calculations, respectively. The SOC effect was included in the band structure calculations. To study the FSs, the maximally localized Wannier functions' method [41,42] was employed.

As illustrated in Fig. 1(a), BaX_4 belongs to the space group I_4/mmm (No. 139). Figures 1(b) and 1(c) exhibit the pictures of grown single crystals for $BaGa_4$ and $BaIn_4$, respectively. The single crystal XRD patterns illustrated in Fig. 1(d) reveal the (00l) crystalline surface of BaX_4. Figures 1(e) and 1(f) display the powder XRD patterns (powder was obtained by crushing single crystals) which can be well refined with the space group I_4/mmm, and the refined lattice parameters are $a = b = 4.57$ Å, $c = 10.78$ Å for $BaGa_4$ and $a = b = 4.97$ Å, $c = 11.98$ Å for $BaIn_4$, respectively. $BaIn_4$ is quite air sensitive, whose surface turned gray when it was exposed in the air for less than one minute. The hump around 20° in $BaIn_4$ presented in Fig. 1(f) is due to the Kapton film which is employed to prevent the sample from decomposing during the acquisition of the patterns. See Supplemental Material for detailed procedure of measurements on $BaIn_4$ [43].

III. RESULTS AND DISCUSSION

A. Large MR in BaX_4

The temperature-dependent resistivity ρ_{xx} with $B//[00l]$ configuration of $BaGa_4$ and $BaIn_4$ are shown in Figs. 2(a) and 2(c), respectively, which demonstrate the metallic behaviors of BaX_4. The resistivity of $BaGa_4$ is comparable with the values reported in previous work [32]. The large residual resistance ratio (RRR) is about 98 for $BaGa_4$ and 244 for $BaIn_4$, indicating high quality of the single crystals. Besides, evident oscillations are observed at 2 K under high magnetic field, as shown in Fig. 2(d), which also demonstrates the high quality of $BaIn_4$. The magnetic field dependence of MR $= (\rho(B) - \rho(0))/\rho(0) = \Delta\rho/\rho_0$ under different temperatures are displayed in Figs. 2(b) and 2(d). Both of them exhibit a large and unsaturated MR which reaches 3×10^3% in $BaGa_4$ and 4×10^4% in $BaIn_4$. The large MR may originate from the carrier compensations and high mobility. The first-principles calculations indicate that the hole and electron concentrations are $n_{h1} = 0.3566 \times 10^{20}$ cm^{-3}, $n_{h2} = 7.6147 \times 10^{20}$ cm^{-3}, and $n_e = 8.1397 \times 10^{20}$ cm^{-3} in $BaGa_4$, $n_h = 3.9449 \times 10^{20}$ cm^{-3} and $n_e = 3.9916 \times 10^{20}$ cm^{-3} in $BaIn_4$, respectively. The nearly perfect compensations $(n_{h1} + n_{h2})/n_e = 0.979$ in $BaGa_4$ and $n_h/n_e = 0.988$ in $BaIn_4$ result in the large MR of BaX_4. The Kohler's rule is sometimes employed as a method to examine the existence of carrier compensation. As shown in Figs. 2(b) and 2(d), the curves of MR versus B/ρ_0 with different temperatures deviate from single line as expected, suggesting the violation of Kohler's rule. However, the violation of Kohler's rule does not rule out the existence of carrier compensation. According to Kohler's rule [44],

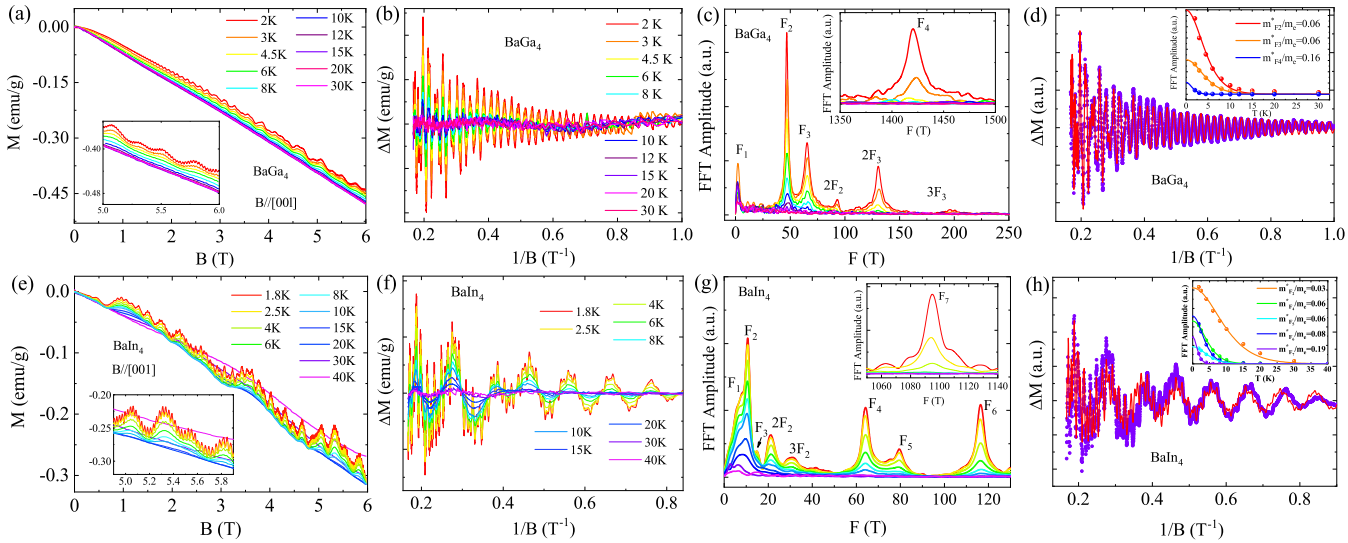

FIG. 3. Evident dHvA oscillations under different temperatures with $B//[001]$ configuration in (a) $BaGa_4$ and (e) $BaIn_4$, respectively. (b),(f) The amplitude of dHvA oscillations plotted as a function of $1/B$. (c),(g) FFT spectra of the oscillations. (d),(h) The multiband LK formula fits (red lines) of oscillations at 2 K. The insets are the temperature dependence of relative FFT amplitude of the main oscillations.

with only one relaxation rate, the MR increases with the increasing magnetic field, which satisfies a universal function $\mathrm{MR} = F(B/\rho_0)$ at all temperatures and fields. It is known that Kohler's rule is applicable to the single-band system. Considering the calculations and dHvA oscillation results, there exists more than one type of carries in BaX_4, the relaxation rates and carrier density of which are different and temperature dependent, breaking the validity of Kohler's rule [45]. For the measurements of Hall resistivity, in order to eliminate the influence of longitudinal resistivity induced by the misalignment of asymmetrical voltage probe, the Hall resistivity can be obtained by taking the difference of data under positive and negative magnetic field. The Hall measurements of BaX_4 have been tried for several times but symmetrical data were unexpectively obtained, in which the weak Hall signal may be obscured by the large MR.

B. dHvA oscillations and the first-principles calculations in BaX_4

Quantum oscillation experiment provides an effective method to study topological properties. Evident dHvA quantum oscillations are observed in $BaGa_4/BaIn_4$ at low temperature and high magnetic field with $B//[00l]$ configuration [Fig. 3(a), Fig. 3(e)]. Both of these compounds show a diamagnetic signal with prominent quantum oscillations. The periodic oscillations $\Delta M = M - < M >$ are obtained after subtracting a smooth background, which are plotted as a function of $1/B$ in Fig. 3(b) for $BaGa_4$ and Fig. 3(f) for $BaIn_4$, respectively. The quantum oscillatory component can be described by LK formula [46,47],

$$\Delta M \propto B^{1/2} \frac{\lambda T}{\sinh(\lambda T)} e^{-\lambda T_D} \sin\left[2\pi\left(\frac{F}{B} - \frac{1}{2} + \beta + \delta\right)\right] \quad (1)$$

$$T_D = \frac{\hbar}{2\pi k_B \tau} \quad (2)$$

$$\mu_s = \frac{e\tau}{m^*}, \quad (3)$$

where $\lambda = (2\pi^2 k_B m^*)/(\hbar e B)$, and T_D is the Dingle temperature. $\beta = \Phi_B/2\pi$ and Φ_B is the Berry phase. The phase shift δ is determined by the dimensionality, $\delta = 0$ and $\delta = \pm 1/8$ for 2D and 3D system, respectively. τ is the quantum scattering time, and m^* is the effective mass. In $BaGa_4/BaIn_4$, four/seven frequencies are extracted from the fast Fourier transform (FFT) analysis, which are presented in Figs. 3(c) and 3(g). Berry phases $\Phi_B = 2\pi\beta$ are both extracted from the multiband LK fittings and Landau level (LL) index fan diagram, the results of which are illustrated in Figs. 3(d) and 3(h) and Figs. S9 and S10, respectively. The corresponding values are listed in Table SI of Supplemental Material [43]. The thermal damping term $R_T = (\lambda T)/\sinh(\lambda T)$ in LK formula is employed to fit the temperature dependence of the oscillation amplitude, as shown in the inset of Figs. 3(d) and 3(h). The light effective masses are obtained from the fittings, which are summarized in Table I. The quantum scattering time τ and quantum mobility μ_s can be estimated according to the Dingle temperature T_D obtained from the LK fittings, as listed in Table I. As shown, BaX_4 has the high quantum mobility in a range of $(0.1 \sim 6) \times 10^4$ cm^2 V^{-1} s^{-1}, as large as the same amplitude in Cd_3As_2 [48,49]. Experimentally, these Dirac-like carriers owning light effective masses and high quantum mobility indicate their linear band dispersion and possible nontrivial topological characteristics.

The first-principles calculations are also employed to examine the topological characteristics in BaX_4. Figure 4(a) shows the band structures of $BaGa_4$ with the SOC included. There are two valence bands and one conduction band crossing the Fermi level. Several Dirac points are obtained in the absence of SOC, while some of them except for the robust Dirac point labeled as D open small gaps (about 7.3 meV to 29.88 meV) in the presence of SOC, as marked with blue circles in Fig. 4(a). The small gaps which almost have no

TABLE I. The parameters extracted from dHvA oscillations in BaX_4. F is the frequency. m^* is the effective mass. T_D is the Dingle temperature. τ is the quantum scattering time. μ is the quantum mobility.

	F (T)	m^*/m_e	T_D (K)	τ (10^{-13} s)	μ_s (10^4 cm^2 V^{-1} s^{-1})
	F_1 1.6	/	/	/	/
	F_2 46.8	0.06	1.77	6.87	2.01
$BaGa_4$	F_3 65.4	0.06	9.81	1.24	0.36
	F_4 1420.3	0.16	11.11	1.09	0.12
	F_1 6.7	/	/	/	/
	F_2 10.7	0.03	1.14	10.63	6.23
	F_3 14.9	/	/	/	/
$BaIn_4$	F_4 64.2	0.06	3.51	3.46	1.02
	F_5 79.5	0.06	15.4	0.79	0.23
	F_6 116.4	0.08	3.45	3.52	0.77
	F_7 1094.9	0.19	6.17	1.97	0.18

influences on the topological properties in magnetotransport measurements are negligible. The robust Dirac point locates at 0.627 eV above Fermi level. Two crossing bands around this Dirac point belong to the different irreducible representations, respectively, which indicates that this Dirac point is a true Dirac point protected by the C_{4v} double group symmetry. The hole-type and the electron-type FSs are shown in Figs. 4(b) to 4(d), respectively. The band structures and FSs of $BaIn_4$ with SOC are shown in Fig. 5. There is one valence band and one conduction band crossing the Fermi level in $BaIn_4$, as shown in Fig. 5(a). Similarly, $BaIn_4$ also possesses several Dirac points in the absence of SOC, and some of them except for the robust Dirac point labeled as 'D' open gaps (about 5.25 meV to 34.43 meV) in the presence of SOC, which are

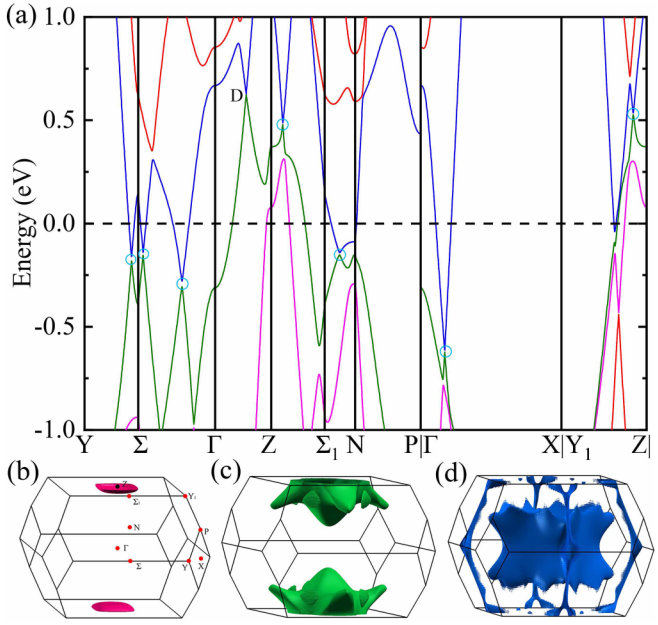

FIG. 4. (a) Band structures along high-symmetry paths of Brillouin zone. The hole-type (b),(c) and electron-type (d) FSs of $BaGa_4$ with SOC included. The blue circles represent the Dirac points with small gaps. The letter D denotes the robust Dirac point.

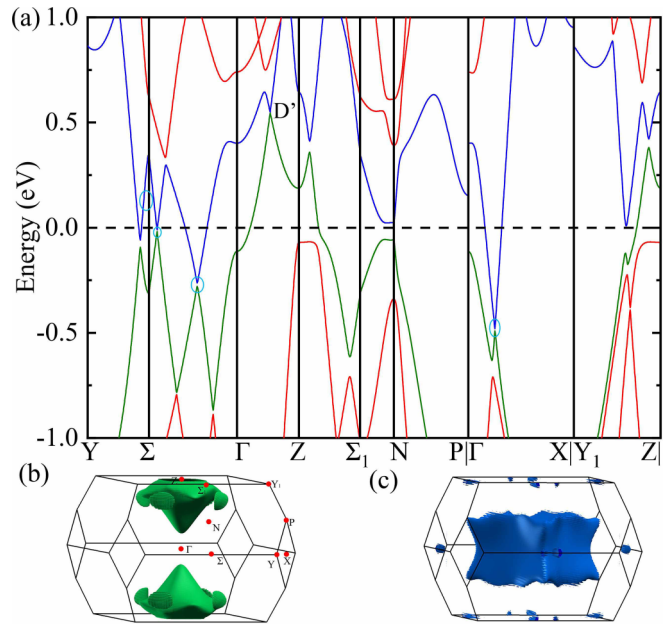

FIG. 5. (a) Band structures along high-symmetry paths of Brillouin zone. The hole-type (b) and electron-type (c) FSs of $BaIn_4$ with SOC included. The blue circles represent the Dirac points with small gaps. The letter 'D' denotes the robust Dirac point.

so small that they have no influences on the topological properties in magnetotransport measurements. The hole-type and electron-type FSs are displayed in Figs. 5(b) and 5(c), respectively. The Z_2 invariants of BaX_4 are studied by calculating the product of the parities of occupied states at eight time-reversal invariant points [50,51] (see Supplemental Material [43]). The calculated Z_2 invariants equal 1, which shows the nontrivial topological characteristics of BaX_4, consistent with previous theoretical study [52]. Compared with homologous compounds $CaAl_4$ with the space group $C2/m$ [53,54], BaX_4 with the space group $I4/mmm$ possesses higher symmetry, leading to the existence of robust Dirac points protected by the C_{4v} double group symmetry. As shown in Figs. 4(a) and 5(a), the overall band structures of BaX_4 display multiple densely arranged Dirac-like points over a large energy range (from -1 eV to 1 eV), which contribute to the magnetotransport. Remarkably, the bands in the vicinity of these Dirac-like points show quasilinear dispersions. Even though they have small gaps, the carriers filling in the quasilinear bands act as Dirac fermions. Moreover, the steep quasilinear dispersions mean the high carrier mobilities, which is verified by estimated carrier quantum mobilities from dHvA oscillations, leading to the large MR of $BaIn_4$ ($\sim 4 \times 10^4\%$) and $BaGa_4$ ($\sim 3 \times 10^3\%$). To identify the Fermi surfaces for each frequency, the angle-dependent dHvA oscillations measurements are conducted and the comparsion between experiments and calculations are carried out. The corresponding Berry phase is also analyzed.

C. The comparison of cross sections between the angle-dependent oscillations and calculations in $BaGa_4$

The angle-dependent dHvA quantum oscillation measurements are conducted with magnetic field B rotating from $B//c$ to $B//ab$ (θ is the angle between the B and c axis), as

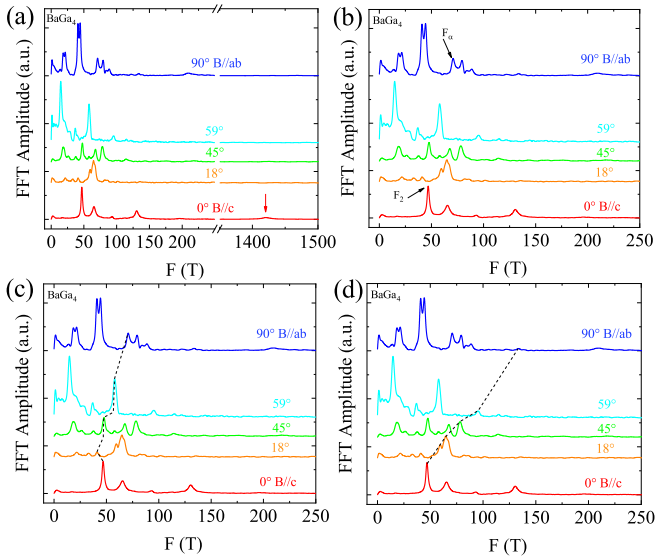

FIG. 6. (a) The FFT spectra of dHvA oscillations with the field in different directions at 2.5 K in $BaGa_4$. Three possible variation trends of frequency F_2 corresponding to the extreme cross section (b) S_6, (c) S_2, and (d) S_8, respectively.

shown in Fig. 6(a) for $BaGa_4$. The frequencies, especially low frequencies, are too complicated to be analyzed. Thus, we focus on the comparison of extreme cross sections of Fermi surfaces with $B//c$ between calculations and experiments. According to the Onsager relation $F = \frac{\hbar}{2\pi e}A_F$, the frequency F in the dHvA oscillations is proportional to the extreme cross sections A_F of Fermi surface normal to the magnetic field. In order to define the corresponding Fermi surface for each frequency, the extreme cross sections of Fermi surfaces with $B//c$ configurations are calculated, which are displayed in Fig. 7 for $BaGa_4$. For comparison, the calculated values and experimental ones are shown in Table II, respectively.

As is shown, in $BaGa_4$, the frequency F_2 may originate from the cross section S_2 of hole Fermi surface or S_6/S_8 of electron Fermi surface. The Fermi surface of S_6 is a long

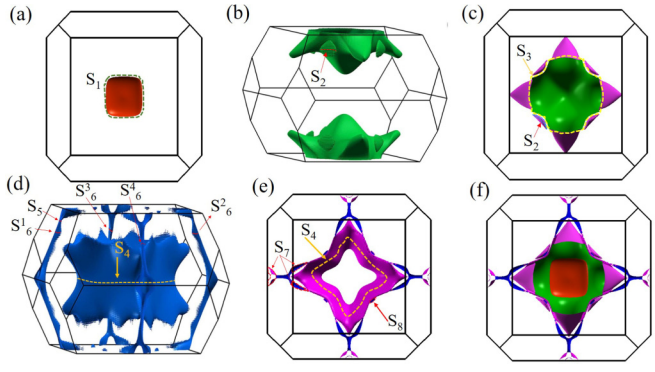

FIG. 7. The sketch map of extreme cross sections of Fermi surfaces with $B//c$ directions in $BaGa_4$. (a),(c) Hole and (e) electron Fermi surfaces projected along the Z-Σ_1 plane of the Brillouin zone. (b),(d) The Fermi surfaces in the 3D Brillouin zone. (f) Total Fermi surfaces projected along the Z-Σ_1 plane. Corresponding cross sections of Fermi surfaces are marked.

TABLE II. The extreme cross sections of Fermi surfaces with $B//c$ configuration from theory and experiments in $BaGa_4$, respectively.

	S_1	S_2	S_3	S_4	S_5	S_6	S_7	S_8
S (10^{-2} Å^{-2})	13.54	0.43	33.59	28.68	0.75	0.44	2.08	0.42
F (T)		F_1		F_2		F_3		F_4
S (10^{-2} Å^{-2})		0.015		0.45		0.62		13.55

strip along Σ-Σ_1 with 2D character. When $B//c$, the extreme cross section $S_6^1 = S_6^2 = S_6^3 = S_6^4 = 0.0044$ Å^{-2} (45.8 T), and when $B//ab$, $S_6^1 = S_6^2 = S_6^3 = S_6^4 = 0.0067$ Å^{-2} (69.7 T). The former corresponds to the F_2 (46.8 T) when $B//c$ and the latter corresponds to the F_α (71.1 T) when $B//ab$, as displayed in Fig. 6(b). Actually, the S_6^3 and S_6^4 increase as B rotating from $\theta = 0°$ to $\theta = 90°$. The S_6^2 increases with the increase of θ until $\theta = 56.6°$, at which the extreme cross section reaches maximum and is infinite, and the extreme cross section decreases as θ further increases. However, the S_6^1 decreases with the increase until $\theta = 33.4°$, at which the extreme cross section reaches minimum (0.0037 Å^{-2}/39.2 T), and the extreme cross section increases as θ further increases. As shown in Fig. 6(b), the frequencies become too complicated to be analyzed as angle changes. The Fermi surface of S_2 is a thin slice, presenting quasi-2D characteristics instead of 3D, the extreme cross section of which may change slightly with the change of θ, as displayed in Fig. 6(c). The Fermi surface of S_8 is an ellipsoid with 3D character, the extreme cross section of which increases with magnetic field rotating from $B//c$ to $B//ab$, as shown in Fig. 6(d). As the frequency F_2 displays three possible variation trends, it may originate from the cross section S_6, S_2, or S_8. Thus, the δ is 0 (for S_2 and S_6) or $-1/8$ (for S_8). The frequency F_3 may originate from S_5 of electron Fermi surface and F_4 from S_1 of the hole Fermi surface, while S_5 is 2D-like and S_1 is 3D-like. The δ equals 0 for F_3 and 1/8 for F_4. The corresponding Berry phases are listed in Table SI [43].

D. The comparison of cross sections between the angle-dependent oscillations and calculations in $BaIn_4$

The angle-dependent dHvA quantum oscillation measurements are also conducted with magnetic field B rotating from $B//c$ to $B//ab$ (θ is the angle between the B and c axis), as shown in Fig. 8 for $BaIn_4$. The extreme cross sections of Fermi surfaces with $B//c$ are calculated and displayed in Fig. 9; the corresponding calculated values and experimental ones are listed in Table III. The frequency F_4 may originate from the cross section S_1 of the hole Fermi surface. The frequency F_6 may originate from the cross section S_4 of electron Fermi surface and the frequency F_7 may be from S_2 of the hole Fermi surface. All of the Fermi surfaces are 3D-like, and the δ equals 1/8 (for F_4 and F_7) or $-1/8$ (for F_6).

However, there exist several extra low frequencies in dHvA oscillations, which may originate from small Fermi surfaces. Considering the flux method of growth, the doping may be introduced, resulting in the Fermi level shift. The extreme

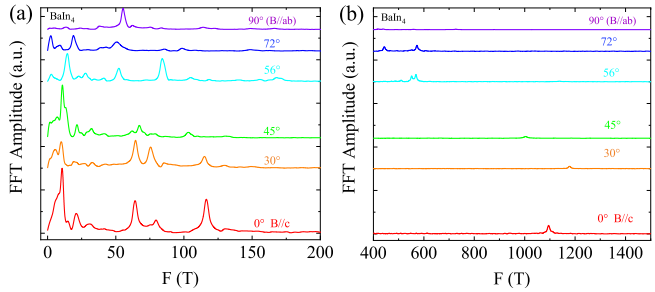

FIG. 8. The FFT spectra of dHvA oscillations with the field in different directions at 1.8 K in $BaIn_4$.

cross sections of Fermi surfaces with the Fermi level shifted 31.9 meV lower are calculated and displayed in Table IV. As shown in Fig. 10(a), except that the Fermi surfaces along Σ-Γ, Γ-Z-Σ_1, and Γ-X get larger or smaller as the Fermi level is shifted, the Fermi surfaces around the Σ point evolve and change from electron type to electron-hole coexisting. The Fermi surfaces S_4 in Fig. 9(c) are connected electron type, while they split into two independent parts when Fermi level is shifted 31.9 meV lower, with one electron type (along Σ-Y) and the other hole type (along Σ-Γ). Thus, the Fermi surfaces S_4 (electron) in Table III evolve into S_4' (electron) and S_5' (hole) in Table IV.

With Fermi level shifted lower, the Frequency F_1 may originate from S_6' (emergent Fermi surface along the non-high-symmetric path in the Z-Γ plane with Fermi level shifted), F_3 from S_4', F_5 from S_1', and F_7 from S_2'. The frequency F_2 may arise from magnetic breakdown [55] corresponding to the adjacent electron Fermi pocket S_4' and hole Fermi pocket S_5' ($S_{F2}^{\text{experiment}}$=$S_4'$-$S_5'$), as shown in the Fig. 10(b). Hence, the Fermi surfaces of $BaIn_4$, especially the smaller ones, can be easily affected by the Fermi level and thus the electronic structures become quite complicated.

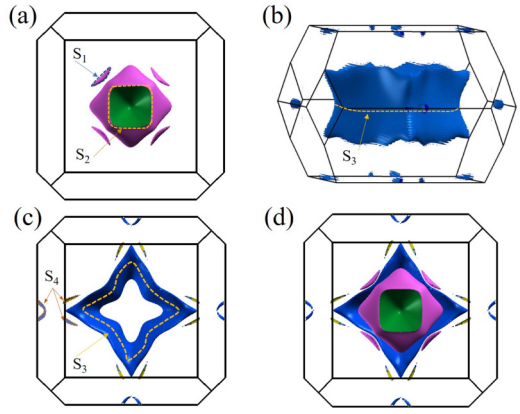

FIG. 9. The sketch map of extreme cross sections of Fermi surfaces with $B//c$ directions in $BaIn_4$. (a) Hole and (c) electron Fermi surfaces projected along the Z-Σ_1 plane of the Brillouin zone. (b) The electron Fermi surfaces in the 3D Brillouin zone. (d) Total Fermi surfaces projected along the Z-Σ_1 plane. Corresponding cross sections of Fermi surfaces are marked.

TABLE III. The extreme cross sections of Fermi surfaces with $B//c$ configuration from theory and experiments in $BaIn_4$, respectively.

	S_1		S_2		S_3		S_4
S (10^{-2} Å^{-2})	0.58		10.30		21.56		1.14
F (T)	F_1	F_2	F_3	F_4	F_5	F_6	F_7
S (10^{-2} Å^{-2})	0.064	0.10	0.14	0.61	0.76	1.11	10.45

E. The Berry phase in BaX_4

The nontrivial Berry phase is defined as the integral of Berry curvature over a closed surface containing the monopole called Weyl point [56], which is usually an important parameter to reflect the topological characteristics of materials in the transport measurements. As noticed, the nontrivial Dirac point D in $BaGa_4$ and D′ in $BaIn_4$ both locate far away from the Fermi level (>500 meV), which contribute little to the magnetotransport properties. Besides, the hole type Fermi surfaces containing nontrivial Dirac point along Γ-Z are not observed in dHvA oscillations. Thus, there is no necessity to discuss the Berry phases of Fermi surfaces corresponding to the D/D′ points. Meanwhile, except for the D/D′ points, the Berry phases of other points in BaX_4 that open gaps after considering the SOC deviate from π in theory, which are consistent with the experiments shown in Table SI [43].

IV. SUMMARY

In conclusion, we have grown high quality single crystals of BaX_4 and investigated their magnetotransport properties. Large and unsaturated MR that reaches 3×10^3% in $BaGa_4$ and 4×10^4% in $BaIn_4$ are presented, which may due to the carrier compensations and high mobility. Prominent dHvA oscillations with multiple frequencies have been observed in BaX_4. Four/seven fundamental frequencies are extracted from the FFT analysis in $BaGa_4$/$BaIn_4$. According to the analysis of the oscillations, light effective masses and high quantum mobilities are obtained, which suggests the possible existence of nontrivial topological characteristics in BaX_4. The first-principles calculations demonstrate that several Dirac points exist in BaX_4 without considering SOC. While in the presence of SOC, some of them open negligible gaps which almost have no influences on topological properties in magnetotransport measurements. The Z_2 invariants of

TABLE IV. The extreme cross sections of Fermi surfaces with $B//c$ configuration from theory with Fermi level shifted down by 31.9 meV and experiments in $BaIn_4$, respectively.

	S_1'	S_2'	S_3'	S_4'	S_5'	S_6'
S (10^{-2} Å^{-2})	0.85	11.40	20.67	0.14	0.035	0.054
F (T)	F_1	F_2	F_3	F_4	F_5	F_6	F_7
S (10^{-2} Å^{-2})	0.064	0.10	0.14	0.61	0.76	1.11	10.45

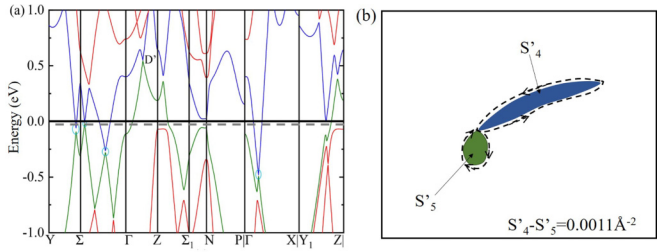

FIG. 10. (a) Band structures along high-symmetry paths. The gray dashed line represents the Fermi level shifted down 31.9 meV. (b) Sketch map for the magnetic breakdown.

BaX_4 equal 1, indicating their nontrivial topological characteristics.

ACKNOWLEDGMENTS

We thank Dr. Peng-Jie Guo for helpful discussions. This work is supported by the National Natural Science Foundation of China (No. 11874422, No. 11574391, No. 11774422, and No. 11774424), the National Key R & D Program of China (No. 2019YFA0308602, No. 2019YFA0308603), and the Fundamental Research Funds for the Central Universities, and the Research Funds of Renmin University of China (No. 18XNLG14, No. 19XNLG18, and No. 19XNLG03). This work is also supported by the Outstanding Innovative Talents Cultivation Funded Programs 2021 of Renmin University of China. Computational resources were provided by the Physical Laboratory of High Performance Computing at Renmin University of China. The FSs were prepared with the XCRYSDEN program [57].

[1] M. Neupane, S.-Y. Xu, R. Sankar, N. Alidoust, G. Bian, C. Liu, I. Belopolski, T.-R. Chang, H.-T. Jeng, H. Lin *et al.*, Nat. Commun. **5**, 3786 (2014).
[2] Z. Liu, J. Jiang, B. Zhou, Z. Wang, Y. Zhang, H. Weng, D. Prabhakaran, S. Mo, H. Peng, P. Dudin *et al.*, Nat. Mater. **13**, 677 (2014).
[3] S. Borisenko, Q. Gibson, D. Evtushinsky, V. Zabolotnyy, B. Büchner, and R. J. Cava, Phys. Rev. Lett. **113**, 027603 (2014).
[4] T. Liang, Q. Gibson, M. N. Ali, M. Liu, R. Cava, and N. Ong, Nat. Mater. **14**, 280 (2015).
[5] C.-Z. Li, L.-X. Wang, H. Liu, J. Wang, Z.-M. Liao, and D.-P. Yu, Nat. Commun. **6**, 10137 (2015).
[6] H. Li, H. He, H.-Z. Lu, H. Zhang, H. Liu, R. Ma, Z. Fan, S.-Q. Shen, and J. Wang, Nat. Commun. **7**, 10301 (2016).
[7] Z. Wang, Y. Sun, X.-Q. Chen, C. Franchini, G. Xu, H. Weng, X. Dai, and Z. Fang, Phys. Rev. B **85**, 195320 (2012).
[8] Z. Liu, B. Zhou, Y. Zhang, Z. Wang, H. Weng, D. Prabhakaran, S.-K. Mo, Z. Shen, Z. Fang, X. Dai *et al.*, Science **343**, 864 (2014).
[9] J. Xiong, S. K. Kushwaha, T. Liang, J. W. Krizan, M. Hirschberger, W. Wang, R. Cava, and N. Ong, Science **350**, 413 (2015).
[10] J. Xiong, S. Kushwaha, J. Krizan, T. Liang, R. J. Cava, and N. P. Ong, Europhys. Lett. **114**, 27002 (2016).
[11] T. Wehling, A. M. Black-Schaffer, and A. V. Balatsky, Adv. Phys. **63**, 1 (2014).
[12] X. Wan, A. M. Turner, A. Vishwanath, and S. Y. Savrasov, Phys. Rev. B **83**, 205101 (2011).
[13] Z. Fang, N. Nagaosa, K. S. Takahashi, A. Asamitsu, R. Mathieu, T. Ogasawara, H. Yamada, M. Kawasaki, Y. Tokura, and K. Terakura, Science **302**, 92 (2003).
[14] H. Weng, C. Fang, Z. Fang, B. A. Bernevig, and X. Dai, Phys. Rev. X **5**, 011029 (2015).
[15] S.-Y. Xu, I. Belopolski, N. Alidoust, M. Neupane, G. Bian, C. Zhang, R. Sankar, G. Chang, Z. Yuan, C.-C. Lee *et al.*, Science **349**, 613 (2015).
[16] S.-M. Huang, S.-Y. Xu, I. Belopolski, C.-C. Lee, G. Chang, B. Wang, N. Alidoust, G. Bian, M. Neupane, C. Zhang *et al.*, Nat. Commun. **6**, 7373 (2015).
[17] B. Lv, H. Weng, B. Fu, X. Wang, H. Miao, J. Ma, P. Richard, X. Huang, L. Zhao, G. Chen *et al.*, Phys. Rev. X **5**, 031013 (2015).
[18] B. Lv, N. Xu, H. Weng, J. Ma, P. Richard, X. Huang, L. Zhao, G. Chen, C. Matt, F. Bisti *et al.*, Nat. Phys. **11**, 724 (2015).
[19] S.-Y. Xu, N. Alidoust, I. Belopolski, Z. Yuan, G. Bian, T.-R. Chang, H. Zheng, V. N. Strocov, D. S. Sanchez, G. Chang *et al.*, Nat. Phys. **11**, 748 (2015).
[20] S.-Y. Xu, I. Belopolski, D. S. Sanchez, C. Zhang, G. Chang, C. Guo, G. Bian, Z. Yuan, H. Lu, T.-R. Chang *et al.*, Sci. Adv. **1**, e1501092 (2015).
[21] N. Xu, H. Weng, B. Lv, C. E. Matt, J. Park, F. Bisti, V. N. Strocov, D. Gawryluk, E. Pomjakushina, K. Conder *et al.*, Nat. Commun. **7**, 11006 (2016).
[22] Z. Liu, L. Yang, Y. Sun, T. Zhang, H. Peng, H. Yang, C. Chen, Y. Zhang, Y. Guo, D. Prabhakaran *et al.*, Nat. Mater. **15**, 27 (2016).
[23] X. Huang, L. Zhao, Y. Long, P. Wang, D. Chen, Z. Yang, H. Liang, M. Xue, H. Weng, Z. Fang *et al.*, Phys. Rev. X **5**, 031023 (2015).
[24] C.-L. Zhang, S.-Y. Xu, I. Belopolski, Z. Yuan, Z. Lin, B. Tong, G. Bian, N. Alidoust, C.-C. Lee, S.-M. Huang *et al.*, Nat. Commun. **7**, 10735 (2016).
[25] F. Arnold, C. Shekhar, S.-C. Wu, Y. Sun, R. D. Dos Reis, N. Kumar, M. Naumann, M. O. Ajeesh, M. Schmidt, A. G. Grushin *et al.*, Nat. Commun. **7**, 11615 (2016).
[26] J. Liu, J. Hu, Q. Zhang, D. Graf, H. B. Cao, S. Radmanesh, D. Adams, Y. Zhu, G. Cheng, X. Liu *et al.*, Nat. Mater. **16**, 905 (2017).
[27] S. Borisenko, D. Evtushinsky, Q. Gibson, A. Yaresko, K. Koepernik, T. Kim, M. Ali, J. van den Brink, M. Hoesch, A. Fedorov *et al.*, Nat. Commun. **10**, 3424 (2019).
[28] Y.-Y. Wang, S. Xu, L.-L. Sun, and T.-L. Xia, Phys. Rev. Materials **2**, 021201 (2018).
[29] R. Kealhofer, S. Jang, S. M. Griffin, C. John, K. A. Benavides, S. Doyle, T. Helm, P. J. Moll, J. B. Neaton, J. Y. Chan *et al.*, Phys. Rev. B **97**, 045109 (2018).
[30] S. Xu, J.-F. Zhang, Y.-Y. Wang, L.-L. Sun, H. Wang, Y. Su, X.-Y. Wang, K. Liu, and T.-L. Xia, Phys. Rev. B **99**, 115138 (2019).

[31] Y.-P. Zhang, X.-Y. Sun, J.-H. He, R.-G. Ling, and S.-X. Liu, J. Struct. Chem. **8**, 99 (1989).
[32] A. Nakamura, T. Uejo, H. Harima, S. Araki, T. C. Kobayashi, M. Nakashima, Y. Amako, M. Hedo, T. Nakama, and Y. Ōnuki, J. Alloy. Compd. **654**, 290 (2016).
[33] M. Wendorff and C. Röhr, Z. Anorg. Allg. Chem. **631**, 338 (2005).
[34] K. Wang, R. Mori, Z. Wang, L. Wang, J. H. S. Ma, D. W. Latzke, D. E. Graf, J. D. Denlinger, D. Campbell, B. A. Bernevig *et al.*, npj Quantum Mater. **6**, 28 (2021).
[35] P. E. Blöchl, Phys. Rev. B **50**, 17953 (1994).
[36] G. Kresse and D. Joubert, Phys. Rev. B **59**, 1758 (1999).
[37] G. Kresse and J. Hafner, Phys. Rev. B **47**, 558 (1993).
[38] G. Kresse and J. Furthmüller, Comp. Mater. Sci. **6**, 15 (1996).
[39] G. Kresse, Phys. Rev. B **54**, 11169 (1996).
[40] J. Perdew, K. Burke, and M. Ernzerhof, Phys. Rev. Lett. **78**, 1396 (1996).
[41] N. Marzari and D. Vanderbilt, Phys. Rev. B **56**, 12847 (1997).
[42] I. Souza, N. Marzari, and D. Vanderbilt, Phys. Rev. B **65**, 035109 (2001).
[43] See Supplemental Material at http://link.aps.org/supplemental/10.1103/PhysRevB.104.205119 for the LL index fan diagram of BaX_4, Berry phases in BaX_4, the detailed measurements process of $BaIn_4$, and the Z_2 invariant of BaX_4.
[44] L. Forró, K. Biljaković, J. R. Cooper, and K. Bechgaard, Phys. Rev. B **29**, 2839 (1984).
[45] R. H. McKenzie, J. Qualls, S. Han, and J. Brooks, Phys. Rev. B **57**, 11854 (1998).
[46] D. Shoenberg, *Magnetic oscillations in metals* (Cambridge University Press, Cambridge, 2009).
[47] Y. Ando, J. Phys. Soc. Jpn **82**, 102001 (2013).
[48] J. Cao, S. Liang, C. Zhang, Y. Liu, J. Huang, Z. Jin, Z.-G. Chen, Z. Wang, Q. Wang, J. Zhao *et al.*, Nat. Commun. **6**, 7779 (2015).
[49] L. He, X. Hong, J. Dong, J. Pan, Z. Zhang, J. Zhang, and S. Li, Phys. Rev. Lett. **113**, 246402 (2014).
[50] L. Fu, C. L. Kane, and E. J. Mele, Phys. Rev. Lett. **98**, 106803 (2007).
[51] L. Fu and C. L. Kane, Phys. Rev. B **76**, 045302 (2007).
[52] T. Zhang, Y. Jiang, Z. Song, H. Huang, Y. He, Z. Fang, H. Weng, and C. Fang, Nature (London) **566**, 475 (2019).
[53] H. Zogg and P. Schwellinger, J. Mater. Sci. **14**, 1923 (1979).
[54] G. J. Miller, F. Li, and H. F. Franzen, J. Am. Chem. Soc. **115**, 3739 (1993).
[55] C.S.A. Muller, T. Khouri, M.R. vanDelft, S. Pezzini, Y.T. Hsu, J. Ayres, M. Breitkreiz, L.M. Schoop, A. Carrington, N.E. Hussey, and S. Wiedmann, Phys. Rev. Research **2**, 023217 (2020).
[56] D. Xiao, M.-C. Chang, and Q. Niu, Rev. Mod. Phys. **82**, 1959 (2010).
[57] A. Kokalj, Comp. Mater. Sci. **28**, 155 (2003).